JGR Solid Earth

RESEARCH ARTICLE
10.1029/2018JB016957

Comparing EGF Methods for Estimating Corner Frequency and Stress Drop From *P* Wave Spectra

Peter M. Shearer[1], Rachel E. Abercrombie[2], Daniel T. Trugman[3], and Wei Wang[1]

[1]Scripps Institution of Oceanography, University of California, San Diego, La Jolla, CA, USA, [2]Department of Earth and Environment, Boston University, Boston, MA, USA, [3]Los Alamos National Laboratory, Los Alamos, NM, USA

Key Points:
- Empirical Green's function (EGF) approaches to resolve earthquake corner frequency suffer from parameter trade-offs
- The spectral ratio method for estimating corner frequency produces biased results if the smaller event corner frequency is unconstrained
- Relative stress drop estimates in compact seismicity clusters are well resolved and show changes in average stress drop over short distances

Correspondence to:
P. M. Shearer,
pshearer@ucsd.edu

Citation:
Shearer, P. M., Abercrombie, R. E., Trugman, D. T., & Wang, W. (2019). Comparing EGF methods for estimating corner frequency and stress drop from *P* wave spectra. *Journal of Geophysical Research: Solid Earth*, *124*, 3966–3986. https://doi.org/10.1029/2018JB016957

Received 30 OCT 2018
Accepted 22 MAR 2019
Accepted article online 2 APR 2019
Published online 25 APR 2019

Abstract Empirical Green's functions (EGFs) are widely applied to correct earthquake spectra for attenuation and other path effects in order to estimate corner frequencies and stress drops, but these source parameter estimates often exhibit poor agreement between different studies. We examine this issue by analyzing a compact cluster of over 3,000 aftershocks of the 1992 Landers earthquake. We apply and compare two different analysis and modeling methods: (1) the spectral decomposition and global EGF fitting approach and (2) a more traditional EGF method of modeling spectral ratios. We find that spectral decomposition yields event terms that are consistent with stacks of spectral ratios for individual events, but source parameter estimates nonetheless vary between the methods. The main source of differences comes from the modeling approach used to estimate the EGF. The global EGF-fitting approach suffers from parameter trade-offs among the absolute stress drop, the stress drop scaling with moment, and the high-frequency falloff rate but has the advantage that the relative spectral shapes and stress drops among the different events in the cluster are well resolved even if their absolute levels are not. The spectral ratio approach solves for a different EGF for each target event without imposing any constraint on the corner frequency, f_c, of the smaller events, and so can produce biased results for target event f_c. Placing constraints on the small-event f_c improves the performance of the spectral ratio method and enables the two methods to yield very similar results.

1. Introduction

Earthquake stress drop is a fundamental source parameter; it relates earthquake moment to rupture dimension and strongly influences the strength of high-frequency ground motion. However, stress drop is difficult to measure accurately for earthquakes where the rupture dimension must be estimated from the radiated seismic waves rather than by more direct measurements. In such cases, a popular approach is to compute Brune-type stress drops (Brune, 1970) from *P* or *S* corner frequencies obtained by fitting a smooth function to the observed body wave displacement spectra, and then using a dynamic rupture model to estimate stress drop. A commonly applied analytical function, providing an idealized representation of the source spectrum, has the form

$$u_P(f) = \frac{\Omega_0}{\left[1 + (f/f_c)^{\gamma n}\right]^{1/\gamma}} \quad (1)$$

where $u_P(f)$ is the model-predicted displacement spectrum, Ω_0 is the long period spectral level, f_c is the corner frequency, n is the high-frequency falloff rate, and γ is a parameter that controls the sharpness of the bend in the spectrum near f_c (e.g., $\gamma = 1$ for the Brune model; $\gamma = 2$ for the sharper corner of the Boatwright, 1980, model). Both models are in common use; larger-scale inversions (e.g., Shearer et al., 2006) typically use the Brune model, but studies modeling individual events and ratios often find the Boatwright model fits the data better (e.g., Abercrombie et al., 2016; Huang et al., 2016). When the corner frequency is in the center of the frequency range of the data, the Brune and Boatwright models give similar results for f_c, but the different curvature in the models near the corner leads to systematic differences when f_c is near or outside the limits of the frequency range (e.g., Abercrombie et al., 2016).

Most authors assume a circular crack model (Eshelby, 1957), for which stress drop can be estimated from corner frequency using

$$\Delta\sigma = \frac{7}{16}\left(\frac{\bar{f}_c}{k\beta}\right)^3 M_0 \tag{2}$$

where $\Delta\sigma$ is stress drop, $\bar{f}_c$ is spherically averaged corner frequency, β is the shear wave speed at the source, M_0 is the seismic moment (proportional to Ω_0), and k is a constant that depends on the wave type (P or S) and specific theoretical rupture model (e.g., Brune, 1970; Kaneko & Shearer, 2014, 2015; Madariaga, 1976; Sato & Hirasawa, 1973). Madariaga (1976) has been the most widely applied model in stress drop analyses, so for ease in comparing with other studies, here we will use his P wave k value of 0.32.

Stress drops computed using equation (2) typically exhibit large scatter and stress drop estimates of specific earthquakes often have relatively poor agreement between different studies (e.g., see discussion in Abercrombie, 2014; Shearer et al., 2006). Some of the variability among studies simply reflects differences in the assumed k value (e.g., Brune vs. Madariaga, P or S phase, assumed rupture velocity); note that these differences, along with any errors in $\bar{f}_c$, are cubed when calculating $\Delta\sigma$. Here we focus on the more fundamental observational question of how corner frequency can be measured most reliably from body wave spectra and what may account for disagreements in $\bar{f}_c$ estimates from different approaches. The key challenge is to remove path and site effects from the observed spectra, so as to obtain unbiased source spectra from which f_c can then be estimated.

The observed seismogram is the convolution of the pulse leaving the source and the source-receiver Green's function (here assumed to include any uncorrected instrument response effects). This can be expressed as a sum in the log frequency domain:

$$A_j = U_j + G_j \tag{3}$$

where A_j is the observed log displacement spectrum at the jth station, U_j is the log spectrum of the pulse leaving the source toward station j, and G_j is the log of the source-receiver response spectrum. If we have an estimate of the log Green's function, G'_j, we can write

$$U'_j = A_j - G'_j \tag{4}$$

where U'_j is the estimated log spectrum of the source pulse. Using equation (1), we can then solve for the best fitting values of Ω_0 and f_c for each station (n and γ are typically fixed to the same values for all spectra analyzed, although this is not required). However, often the log spectra are first averaged over all stations recording the event, that is,

$$\bar{U}' = \sum_{j=1}^{n_j} U'_j / n_j \tag{5}$$

where n_j is the number of stations. In practice, this averaged (stacked) spectrum is generally smoother than the individual station spectra and can be fit more closely using equation (1). Synthetic rupture experiments have shown that the corner frequency estimated from the spectral stack $\bar{U}'$ provides a good approximation to the average of the individual station corner frequencies (Kaneko & Shearer, 2014, 2015). However, this corner frequency will only approximate the true spherical average, $\bar{f}_c$, required in equation (2) and significant errors in $\bar{f}_c$ and inferred stress drop are likely when only a small number of stations are used (Kaneko & Shearer, 2014, 2015).

Because the attenuation and velocity structure are usually not known well enough to estimate G'_j directly, an empirical approach is typically applied to estimate the source-to-receiver response (termed the empirical Green's function or EGF). These empirical methods require that multiple earthquakes (at least two) are located close enough to each other that G_j can be assumed constant for all events. In this case we have

$$A_{ij} = U_{ij} + G_j \tag{6}$$

where i is the event index. Ideally, the EGF could be obtained by using the spectrum of a small earthquake of very short rupture duration, such that its true source spectrum is flat across the observation band (Mori &

Frankel, 1990; Mueller, 1985). In this case $U_{ij} = 0$ and the EGF for station j is simply the observed spectrum of the small event:

$$G'_j = A_j(\text{small earthquake}) \tag{7}$$

Once computed, G'_j can then be used to correct the observed spectra of larger earthquakes.

However, in practice, earthquakes small enough to have a truly flat spectrum over the desired bandwidth typically have signals too weak to have acceptable signal-to-noise ratio (SNR). Thus, it becomes necessary to account for the spectral shape of all the earthquakes being modeled, including the smallest events. This is generally done by using equations (1) and (6) together to fit the observed spectra of both large and small earthquakes. Different studies have used a variety of approaches, on different scales with different constraints, ranging from analyzing closely located pairs of events (e.g., Abercrombie, 2014, 2015; Abercrombie et al., 2016; Huang et al., 2016), to earthquake clusters (e.g., Andrews, 1986; Baltay et al., 2010, 2011; Hough, 1997; Ide et al., 2003; Imanishi & Ellsworth, 2006; Kwiatek et al., 2014) to larger-scale inversion (e.g., Bindi et al., 2009; Oth et al., 2011; Pacor et al., 2015; Shearer et al., 2006; Trugman & Shearer, 2017).

In practice, all methods are subject to the limitations in the data, including the number of stations, the magnitude range of the earthquakes, the frequency range of the recorded signals above the noise level, and the appropriateness of the simplified source models that are generally assumed. EGF approaches may differ in their event and station selection criteria, the extent to which modeling is performed separately for given target events and selected EGF events or simultaneously for groups or clusters of events, and whether any constraints are placed on small-earthquake corner frequency.

Our goal here is not to test all of the different methods, but to explore why two end-member approaches can produce different results when applied to the same data set. We compare two contrasting approaches to this problem of empirical source spectral estimation: (1) the spectral decomposition and global EGF fitting method (e.g., Shearer et al., 2006; Trugman & Shearer, 2017) and (2) the spectral ratio fitting method (developed by Abercrombie et al., 2016; Ruhl et al., 2017). The spectral decomposition approach has typically been applied to large data sets spanning a range of magnitudes and the spectral ratio method to target events of interest using specially selected smaller-magnitude EGF events. To facilitate a comparison between the methods, we will apply the spectral ratio approach to a fixed set of smaller-magnitude events that are also included in the spectral decomposition analysis. Later, we will discuss the implications of our results for the methods as they are more normally applied, as well as to other EGF-based approaches.

We apply both methods to a dense cluster of about 3,000 earthquakes in Southern California that is small enough (<6 km across, horizontally and vertically) compared to the station distribution that a constant EGF to each station is a reasonable assumption. In this way, we can compare the different analysis methods with less ambiguity regarding the source of any differences. We focus on the uncertainties in the EGF and corner frequency estimates and explore the origins of differences in results between the two approaches. We find that uncertainties in the global EGF imply that the relative values of corner frequency (and inferred stress drop) are much better constrained than their absolute values. The EGF uncertainties are related to trade-offs between the best fitting values of high-frequency falloff rate n, non-self-similar scaling of f_c with moment, and the median stress drop. The spectral ratio fitting approach, at least for this data set, yields greater scatter in its results for f_c than the global EGF approach, due to a less constrained inversion process. The two methods can be brought into good agreement by imposing a constraint on the assumed corner frequency of the smaller events used in computing the spectral ratio.

1.1. Spectral Decomposition and Global EGF Fitting

When each earthquake is recorded by multiple stations and each station records multiple earthquakes, it is possible to decompose the observed spectra into best fitting event, station, and distance-dependent (or traveltime dependent) components (e.g., Andrews, 1986; Bindi et al., 2009; Oth et al., 2011; Shearer et al., 2006; Trugman & Shearer, 2017). This can be done purely from the data without assuming any theoretical model for the source spectra or attenuation function, most commonly by working with log(amplitude) spectra and expressing the observed log spectra as the sum of the different terms, that is,

$$A_{ij} = e_i + s_j + t_{k(i,j)} + r_{ij} \tag{8}$$

where A_{ij} is the observed log displacement spectrum for event i and station j, e_i is the event term, s_j is the station term, t_k is a term that depends upon the source-receiver traveltime, discretized into bins indexed by k,

and r_{ij} is the misfit for path ij. Note that e_i is different from U_{ij} in equation (6) because it represents an average of the source recorded at different stations. The event terms, e_i, describe only relative differences among event spectra because the inversion contains an ambiguity in the absolute spectral shapes (e.g., a constant spectrum of arbitrary shape could be added to the event terms, e_i, and subtracted from the station terms, s_j, without affecting the data fit). To resolve the ambiguity, a single EGF function (termed here the global EGF) is estimated for the entire data set by finding the function that, when subtracted from all the event terms, yields the best fit to a theoretical model of the expected source spectra, as defined by equations (1) and (2). This global EGF function can then be used to correct the individual event terms to obtain estimates of the true source spectra for all of the earthquakes.

Estimating the global EGF function does depend on the misfit criteria and modeling assumptions for the theoretical spectral shape (e.g., high-frequency falloff rate, self-similar, or non-self-similar models) and different parameter choices will yield different results. Recently, Trugman and Shearer (2017) found a strong trade-off between the assumed high-frequency falloff rate and the degree of stress drop scaling with moment for five regions in Southern California. This introduces an uncertainty in the global EGF that translates into uncertainty in the absolute level of the stress drops and their possible scaling with moment. Thus, spectral decomposition and global EGF fitting is most reliable for resolving relative spectral differences among nearby events; it is subject to larger uncertainty when comparing absolute stress drops between different regions, for which a single global EGF is likely inappropriate and separately computed EGFs are poorly constrained owing to parameter trade-offs. This uncertainty is highlighted by large differences in median stress drop for nearby regions in two recent stress drop studies. Oth (2013) estimated median stress drops for the island of Kyushu that are about 10 times higher than the rest of Japan, which is hard to explain from a tectonic perspective (Oth et al., 2017). Trugman and Shearer (2017) found median stress drops for aftershocks of the 1992 Landers earthquake were about 4 times larger than aftershocks of the nearby 1999 Hector Mine earthquake. Such large differences in absolute stress drop between regions would have important implications, but are they truly required by the data, or could they be a result from errors in the estimated global EGFs obtained from the separate inversions?

1.2. Spectral Ratio Fitting

The spectral ratio fitting approach developed by Abercrombie et al. (2016) is a version of the classic EGF methods that have been used for decades (e.g., Frankel, 1982; Mueller, 1985, see Hutchings & Viegas, 2012 for a review). This particular approach was designed to prioritize the appropriateness of the EGF event selection, and its stability by stacking the best EGF events. For each target event of interest, a number of smaller nearby EGF events are selected, based on proximity and cross-correlation criteria. The EGF events are required to be at least one magnitude unit smaller so that the corner frequencies of the two events can be distinguished. The cross correlation is of particular importance when the location uncertainties are larger than the source dimensions of the target earthquakes (Abercrombie, 2015), and when calculating the relative source-time function of the target event, which requires ensuring that the EGF assumption works in phase as well as in amplitude (e.g., Abercrombie et al., 2016). At a given seismic station, the spectral ratio can be computed between the target and EGF event; this is simply the difference of their log spectra. From (1), we expect that this spectral ratio should have the form (e.g., Abercrombie & Rice, 2005)

$$u_{Pr}(f) = u_{P1} - u_{P2} = \Omega_{0r}\left[\frac{1+(f/f_{c2})^{\gamma n}}{1+(f/f_{c1})^{\gamma n}}\right]^{1/\gamma} \tag{9}$$

where $u_{Pr}(f)$ is the predicted spectral ratio of event 1 (target) to event 2 (smaller event), Ω_{0r} is their moment ratio (M_{01}/M_{02}), f_{c1} is the target event corner frequency, and f_{c2} is the smaller-event corner frequency. For each observed spectral ratio, one can find the best fitting values of Ω_{0r},f_{c1}, and f_{c1} (n and γ are typically fixed to the same values for all spectral ratios analyzed, although this is not required).

Note from equation (2) that in the case of constant stress drop (self-similarity), we expect $f_c \propto M_0^{-1/3}$ and thus $f_{c2}/f_{c1} \propto \Omega_{0r}^{1/3}$. Although equation (9) is often used to fit the spectral ratio of two individual spectra (e.g., Abercrombie & Rice, 2005; Huang et al., 2016), to obtain more stable results, Abercrombie et al. (2016) and Ruhl et al. (2017) summed the normalized spectral ratios for each target event with all EGF events, per station and over all stations. Abercrombie (2015) investigated how the choice of EGF affected the results of spectral ratio analysis; she found systematic variation in stress drop as the appropriateness of the EGF decreased, highlighting the importance of EGF event selection. The spectral fitting approach of Abercrombie

et al. (2016) uses the grid search method originally developed by Viegas et al. (2010) to calculate the uncertainties in the corner frequency measurements, and the quality criteria described by Abercrombie (2014) to select ratios with sufficient amplitude range to remove fits biased by source heterogeneity such as that observed by Uchide and Imanishi (2016).

Although the spectral ratio approach might appear to avoid the need to compute an EGF function and thus not be subject to uncertainties in the EGF, in fact, an EGF is implicit in the method. To see this, note that f_{c1} and f_{c2} predict model spectra that will differ from the observed spectra by the underlying EGF function. Thus, misfits between the observed and model-predicted target and EGF event spectra can be expressed as

$$A_1 - P_1 = G + r_1 \tag{10}$$

$$A_2 - P_2 = G + r_2 \tag{11}$$

where A_1 and P_1 are the observed and model-predicted target event log spectra, A_2 and P_2 are the observed and model-predicted EGF event log spectra, G is the true log EGF, and r_1 and r_2 are the residuals (misfit) to the two log spectra. To minimize the residuals, we set G to the average of the differences:

$$G = \left[(A_1 - P_1) + (A_2 - P_2)\right] \tag{12}$$

Alternatively, if A_2 is the result of stacking many different EGF events, it may be desirable to fit the shape of A_2 exactly, in which case $r_2 = 0$ and

$$G = A_2 - P_2 \tag{13}$$

The spectral ratio approach generally uses the smaller earthquakes only as a means to constrain the target event corner frequency; that is, the f_{c2} estimates obtained for the smaller earthquakes are considered too uncertain to use in computing stress drops (e.g., Abercrombie, 2013; Viegas et al., 2010). The analysis is typically applied separately for each target event using a different set of EGF events for each target to maximize the appropriateness of the common path assumption. This has the advantage that the EGF event selection can be optimized for each target event but has the potential disadvantage that there is no self-consistency check between target events that the f_{c2} values or the implicit EGF functions are similar, even when nearly the same set of EGF events is used. Abercrombie (2015) and Ruhl et al. (2017) showed that calculated corner frequencies exhibit increased uncertainty and systematic bias as they approach within a factor of two of the maximum frequency of the signal.

2. Earthquake Data Set and Preprocessing Steps

To compare the two methods and their resolution, we examine a compact cluster of 3,438 aftershocks of the 1992 Landers earthquake in Southern California, as recorded by the Southern California Seismic Network (SCSN) from 1992 to 2000. Using the relocated catalog of Hauksson et al. (2012), we select events within a lat/lon box of (34.1412°, 34.1856°, −116.4490°, and −116.4096°) and from 6- to 12-km depth (see Figure 1). We select the limited box dimensions to avoid any systematic spatial gradients in the observed spectra, which we did observe in a preliminary analysis of a slightly larger region and depth extent. This makes the assumption of a single global EGF in the spectral decomposition analysis reasonable, so that the effects of EGF event selection can be excluded in this comparison. It also makes the spectral decomposition and global EGF approach closer to that of clustered EGF approaches (e.g., Hough, 1997; Kwiatek et al., 2014). Later, we will test the validity of this assumption in more detail.

Most of the earthquakes are from M_L 0.6 to 3, but there are a small number of larger events up to $M_L = 5.5$ (see Figure 1c). We extract waveforms using the Seismic Transfer Protocol tool to obtain vertical-component seismograms (mostly channel EHZ) and phase pick data. We then compute P wave displacement spectra for stations within 100 km and all events of $M_L \geq 0.5$ using the windowing and multitaper method described in Trugman and Shearer (2017). We discard waveforms flagged as likely clipped, reject spectra that have an average SNR less than 3 in each of five frequency bands (2.5–6, 6–10, 10–15, 15–20, and 20–25 Hz), and reject stations that record less than 20 events, and events recorded by less than three stations. This leaves 3,075 events recorded by a total of 59 stations (see Figure 1d). The maximum magnitude of the remaining events is 3.8, as the larger events do not pass the clipping and SNR requirements.

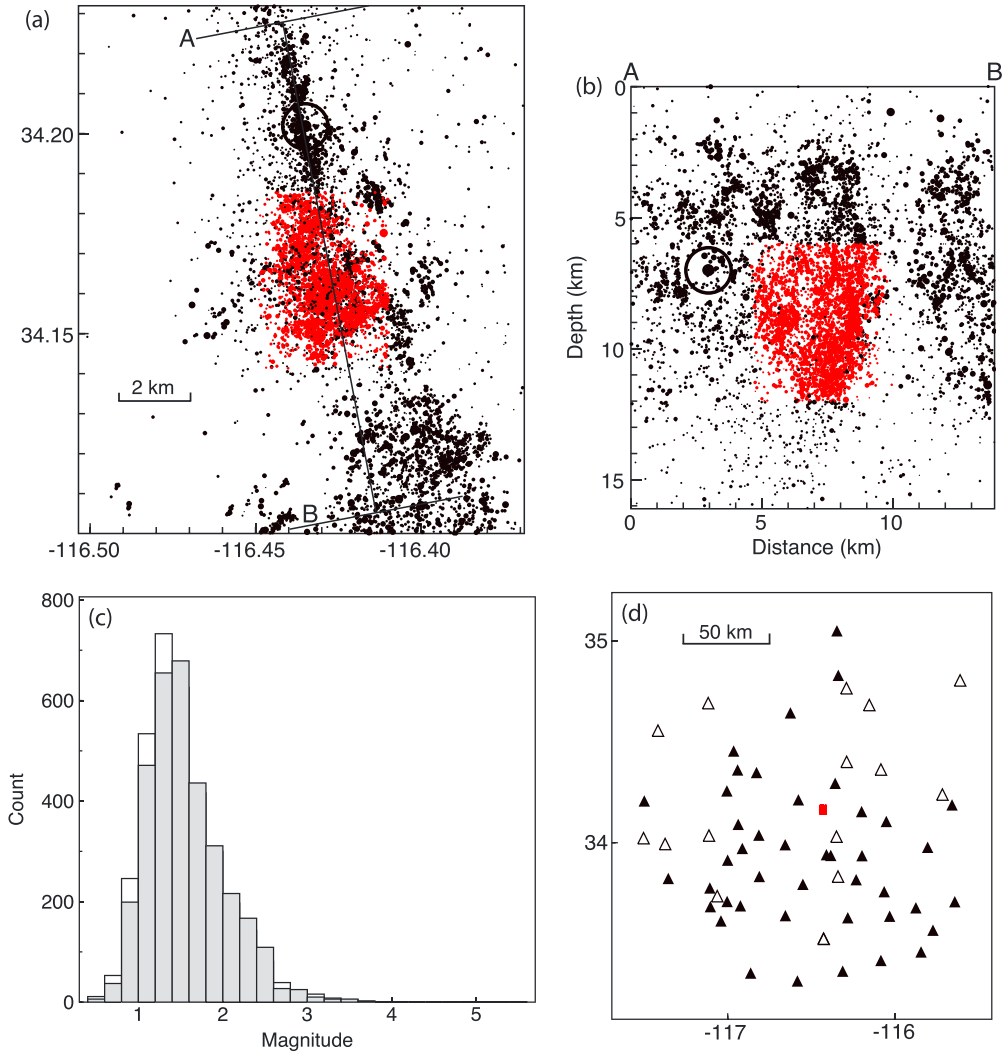

Figure 1. Earthquake and station distribution used in this study. A closeup of 1992–2000 aftershocks of the 1992 Joshua Tree and Landers earthquakes in Southern California, plotted in (a) map view, and (b) cross section along profile AB. The 3,438 earthquakes analyzed in this study are plotted in red, windowed in lat/lon/depth (see text), with surrounding events plotting in black. Symbol sizes are scaled by local magnitude. The *M* 7.3 Landers earthquake epicenter is circled. Locations are from Hauksson et al. (2012). (c) Histogram of earthquake catalog magnitude (M_L); events retained in the analysis are plotted as the gray bars. (d) Southern California Seismic Network station locations (triangles) compared to the earthquake locations (red). Stations recording at least 20 events are plotted in black.

We do not require that the smaller events cross correlate with, or have similar focal mechanisms to, larger target events of interest. Although this is an underlying assumption of the EGF approach in the strictest sense, it is considered less important in the frequency domain and assumed to average out when multiple stations are used (e.g., Boyd et al., 2017; Ross & Ben-Zion, 2016; Shearer et al., 2006). Only 18 mechanisms (A or B quality from Hardebeck & Shearer, 2003) are available for our data set. Retaining all the earthquakes simplifies our analysis and ensures that we use the same set of events for both the global EGF and spectral ratio methods. By maximizing the number of smaller events retained in the analysis, we also increase the likelihood that directivity and other source complexities will be averaged out in fitting their spectra, even with a limited number of stations (Calderoni et al., 2015; Ross & Ben-Zion, 2016).

Our spectra are derived from 1.5-s windows of seismograms with a 0.01 s sample interval and therefore have a frequency spacing of 2/3 Hz. Although the Nyquist frequency is 50 Hz, we restrict the frequency range of our analysis to a maximum of 25 Hz because few of our data have good SNR above that cutoff. Our observed spectra result from a number of choices during processing, including the time window length and

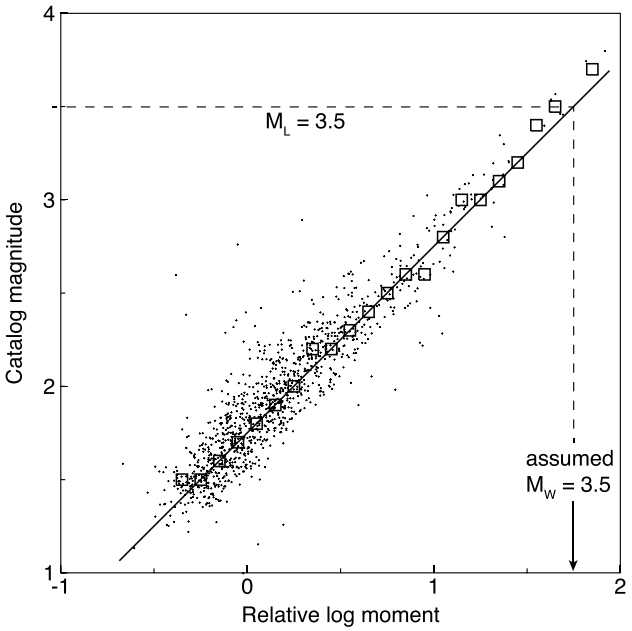

Figure 2. Catalog magnitude M_L versus relative moment from the event terms in the spectral decomposition method. Squares are median M_L in bins of 0.1 in relative moment. The best fitting line (L1 norm) to the squares is shown. By assuming $M_W = M_L$ at M 3.5, the relative moments can be converted to true moments. To reduce the scatter, only event terms defined by six or more stations are plotted, which is why there are few events with catalog magnitudes below 1.2.

position relative to the catalog P wave pick, the multitaper parameters, and the SNR criteria used to reject spectra. However, we have found that these choices have a relatively minor effect on the final results (e.g., corner frequency estimates) compared to differences arising from the EGF approaches used to correct for path effects that are the focus of this paper. Therefore, we do not explore variations in spectral computation details and use exactly the same set of spectra in comparing EGF methods, so that we can be sure that any differences in the final results are due to the methods themselves rather than the spectra input into the methods.

3. Application of Spectral Decomposition and Global EGF Fitting

Our source region is so compact that the path to each receiver is nearly identical, and so the path terms can be entirely absorbed into the station terms. Thus, we simplify equation (8) by removing the traveltime dependent term and obtain

$$A_{ij} = e_i + s_j + r_{ij} \tag{14}$$

As described in Trugman and Shearer (2017), we solve for e_i and s_j using an iterative, robust least squares method where L1 norm weights are used to minimize the influence of any outliers in the spectra.

The resulting event terms, e_j, describe relative differences in the station-averaged spectra at the source. The long-period part of the event terms is proportional to the relative moment of the earthquakes. To obtain an estimate of the true moment of each earthquake, we derive a scaling relation between the event term relative moment and the local earthquake magnitude, as described in Trugman and Shearer (2017) and Shearer et al. (2006). Figure 2 plots catalog magnitude M_L versus the relative log moment, as defined by the average log value of points 5–7 in the spectrum (2.67, 3.33, and 4 Hz). Although in principle this measurement should be made at zero frequency, we have found in practice that frequencies below ~3 Hz yield less reliable results because of SNR limitations for these data, especially for the smaller earthquakes. The best fitting (L1 norm) line has a slope of 1.00 and a local magnitude of 1.75 for zero relative log moment. Note that a slope of 2/3 would be expected if M_L and M_W were always the same. However, as many studies have shown (e.g., Abercrombie, 1996; Hanks & Boore, 1984; Hutton et al., 2010; Munafò et al., 2016; Ross et al., 2016), M_L deviates from M_W for small earthquakes. Because few earthquakes in our data set have independent estimates of moment, we assume that $M_W = M_L$ at $M = 3.5$ for Southern California, consistent with the analysis of Ross et al. (2016), allowing us to obtain true moment estimates for all of our event terms. Note that for simplicity we do not apply the small correction, discussed in Trugman and Shearer (2017), for the expected decrease in the spectral level between 0 and 3.33 Hz (i.e., the spectra are not completely flat at 3.33 Hz). This will lead to a slight underestimation of moment for larger events with $f_c <\sim 4$ Hz, but this will have minimal effect on the corner frequency measurements that are our focus here.

Next, we stack the event terms defined by at least three stations within bins at intervals of 0.25 in relative moment (see Figure 3a). As expected, the event term stacks are uniformly spaced in log amplitude at 3.33 Hz (the reference frequency for our relative moment calculation) but converge at higher frequencies due to lower corner frequencies for the larger earthquakes. The bins plotted have average local magnitudes ranging from 1.03 to 3.43; reflecting the magnitude distribution of the data (see Figure 1c), there are fewer earthquakes at larger magnitudes. Smoother and more stable event term stacks are obtained when there are a large number of contributing earthquakes. The two largest moment bins have 5 and 6 earthquakes, respectively, much less than the other bins and their spectra are rather irregular. Therefore, we do not use these two bins in the EGF fitting that we now describe.

The basic idea is to estimate a "global" EGF function, which, when subtracted from the event term stacks, will yield source spectra that agree with the theoretical spectral shape given by equation (1). As in previous

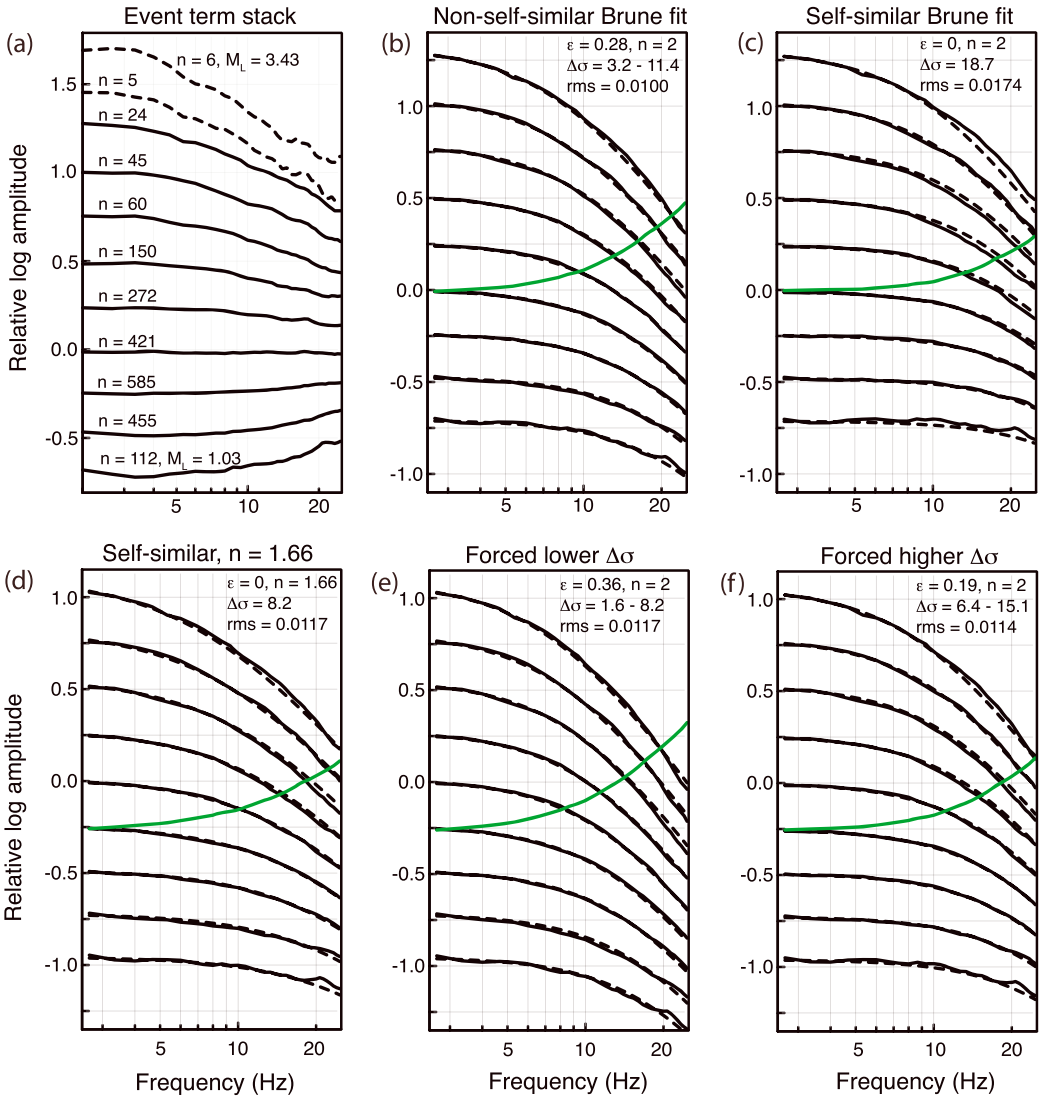

Figure 3. Stacked event term spectra and fits to a global EGF function for the Landers seismicity cluster. (a) Event term stacks from spectral decomposition. Terms are averaged within bins of 0.25 in relative log amplitude (proportional to log moment). The number of contributing earthquakes, n, is labeled, as well as the average local magnitude of the endpoint bins. The dashed lines indicate stacks with less than 10 contributing earthquakes, which are not used for the EGF fitting. (b) The best fitting non-self-similar ($\epsilon \neq 0$) Brune ($n = 2$) model. The global EGF function is plotted in green. The solid lines show the EGF-corrected stacks, and the dashed lines show the model prediction ($\epsilon = 0.28$) in which stress drop increases from 3.3 to 11.4 MPa as a function of moment. The root-mean-square misfit is labeled. (c) The best fitting self-similar ($\epsilon = 0$) Brune model. (d) A self-similar Brune model with a best fitting n value of 1.66. (e) A non-self-similar Brune model in which the stress drop for the smallest moment bin is forced to half its value in panel (b). (f) A non-self-similar model in which the stress drop for the smallest moment bin is forced to twice its value in panel (b). EGF = empirical Green's function.

studies, we use the Brune model (γ =1) as it fits the stacked mean spectra well. To reduce the number of degrees of freedom, we assume that the average source spectra are either self-similar (constant stress drop) or have stress drops that vary smoothly with moment, that is,

$$\log_{10}\Delta\sigma = \epsilon_0 + \epsilon \log_{10}(M_0/M_{0ref}) \tag{15}$$

where $\epsilon_0 = \log_{10}\Delta\sigma$ at the reference moment, M_{0ref}. Note that $\epsilon = 0$ for self-similarity and that positive values of ϵ describe an increase in stress drop with moment. We apply an iterative grid search approach to find the best fitting model parameters (i.e., the parameters that yield the lowest root-mean-square (rms) misfit between the observed and predicted stacked spectra) and associated global EGF correction spectrum.

The inversion results will vary somewhat depending upon the weighting applied. Here we weight by $1/f$ so as to give equal weight in log frequency and better match the visual appearance of the fits in our plots. We also weigh each event term stack equally; that is, we do not assign more weight to bins with more events. We have found that different weighting choices have only a minor effect on our final results, so we do not explore these effects in any detail, and simply apply the same weighting scheme to all of our inversions. For completeness, we also tried fitting the sharper-cornered Boatwright source model to the stacked event spectra but found that this gave a relatively poor fit to the data stacks, regardless of the other parameter choices. Thus, we did not explore the Boatwright model further for fitting the data stacks and estimating the global EGF function, although, as discussed later, some individual event spectra are fit better with the Boatwright model. It is possible that the stacking process tends to round off the sharper corners of single events.

Figure 3b shows the fit obtained for the non-self-similar Brune model ($\gamma = 1$, $n = 2$), which yields a best fitting ϵ of 0.28 and an increase in computed stress drop with moment from 3.2 to 11.4 MPa. The green line shows the global EGF function, which produces the solid lines in Figure 3b when subtracted from the stacks in Figure 3a. Overall, the fit is quite good with a rms misfit of 0.01. Note that the average misfit at each frequency point is zero because any systematic offset would be absorbed into the EGF function. This result agrees closely with the $\epsilon = 0.28$ obtained by Trugman and Shearer (2017) for the Brune model and a larger box of Landers aftershocks, which encompasses the seismicity cluster we consider here.

Next, we test whether a self-similar Brune model can fit the stacked spectra. As shown in Figure 3c, the fit is noticeably worse, with an rms misfit of 0.0174 (i.e., 74% larger than the misfit in Figure 3b). The global EGF function is quite different, resulting in higher corner frequencies and estimated stress drops for each moment bin. However, this does not imply that the model shown in Figure 3b is particularly well constrained, as there are other parameter choices that can result in fits that are almost as good. Three examples are plotted in the bottom row of Figure 3. As discussed in Trugman and Shearer (2017), there is typically a trade-off between the scaling parameter ϵ and the high-frequency falloff rate n. Self-similarity in this case can be preserved if the falloff rate in shallower than 2, as shown in Figure 3d. In this case, the best fitting n is 1.66, $\Delta\sigma$ is constant at 8.2 MPa, and the misfit (0.0117) is only slightly larger than the non-self-similar Brune model. The key observational constraint is that the larger earthquakes in the data set radiate more at high frequencies than a self-similar Brune ($n = 2$) model predicts. This can be explained either with non-self-similar Brune models (i.e., raising f_c for the larger earthquakes) or self-similar $n < 2$ models (i.e., reducing the high-frequency falloff rate). However, even if a fixed $n = 2$ model is assumed, there remains a trade-off between ϵ and the absolute stress drops. This is shown in Figures 3e and 3f, where the stress drop of the smaller moment bin is forced to be half or twice its values in Figure 3b. The fits are only slightly worse, with rms misfits of 0.0117 and 0.0114, respectively. Note that the global EGF function varies greatly for the different models and this has a large effect on the EGF-corrected spectral shapes but not on the misfit.

One approach at this point would be to attempt to assess what level of rms misfit increase is statistically significant given the size of the data set. That is, perhaps it could be shown that despite the similar visual appearance of the fits in the bottom row of Figure 3 to the non-self-similar Brune model of Figure 3b, the increase in rms misfit is large enough that these models can be rejected as unlikely. However, drawing rigorous conclusions is hampered by the likelihood of correlated errors in the data and the difficulty in determining the true number of degrees of freedom in the data stacks. For example, it is clear that the misfits are correlated over some frequency range. Thus, we prefer to only reject models that clearly yield a substantially worse visual fit to the data stacks. It is not our purpose here to explore all of the trade-offs in the parameters, but to use this example to highlight the difficulty in drawing firm conclusions regarding optimal model fits even with a large (3,000 earthquake) data set spanning a factor of 100 in moment, and a factor of 10 in frequency range. The problem is that there are no constraints on the global EGF function and its variations can accommodate a wide range of model parameters. Thus, the absolute value of stress drop, its scaling with moment, and the high-frequency falloff rate are individually rather poorly constrained. To resolve the ambiguity would require a larger magnitude range and a larger signal frequency range than are available for most regional seismic networks.

The question of whether earthquakes are self-similar, implying constant average stress drop with moment, has been widely debated (e.g., Abercrombie, 1995; Abercrombie & Rice, 2005; Andrews, 1986; Baltay et al., 2011; Ide & Beroza, 2001; Ide et al., 2003; Mayeda & Walter, 1996; Prieto et al., 2004). Our results suggesting

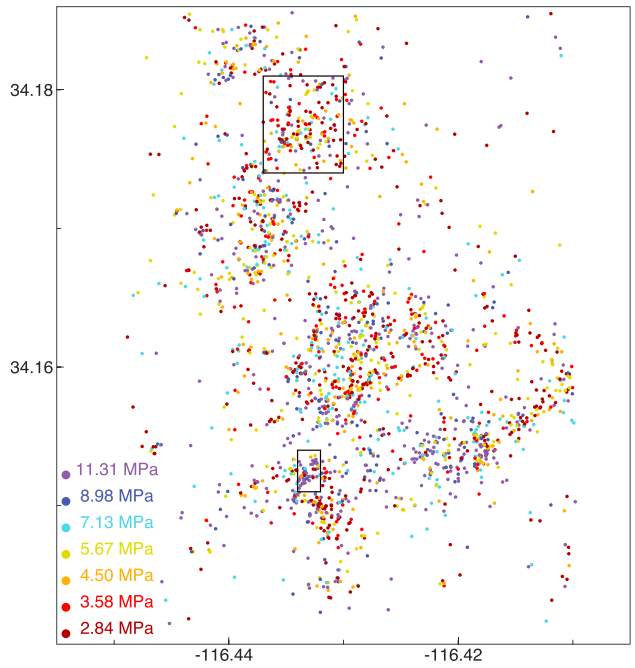

Figure 4. Individual event stress drops for the Landers cluster as estimated from the event terms and the global empirical Green's function of Figure 3b. Rectangles surround example regions with lower-than-average stress drop (northern box) and higher-than-average stress drop (southern box); see text for details.

non-self-similarity (stress drop increasing with moment) over a limited magnitude range for a subset of the Landers aftershocks are consistent with the Trugman and Shearer (2017) study of the entire Landers aftershock sequence. They also found evidence for non-self-similarity in four other areas of seismicity in Southern California. However, as discussed above, non-self-similarity is only required in these results when the high-frequency falloff rate is constrained to $n = 2$, so it is important to consider all the trade-offs between model parameters and the uncertainties in the underlying EGFs before drawing firm conclusions about earthquake scaling issues.

The global EGF approach provides much better constraints on the relative source spectra among different events and on their relative corner frequencies and stress drops than on their absolute values. Once a global EGF is estimated, it can be applied uniformly to correct all the event terms and any error in the EGF will bias all the results in the same way. Figure 4 plots estimated stress drops derived from f_c fits to event terms for 2,124 earthquakes, after correcting for the global EGF function derived for a non-self-similar Brune model (green curve in Figure 3b). Higher stress drops are plotted in blue and lower stress drops in red, a color scheme consistent with the fact that higher stress drops are associated with more high-frequency energy, that is, a bluer spectrum. There is considerable scatter in individual event stress drops, only some of which is explained by the moment scaling, but there appear to be spatially coherent patterns of higher- and lower-than-average stress drop regions. We performed two tests to check if these regional variations are robust as a function of earthquake size. First, we made separate plots for $M_L < 1.6$ and $M_L > 1.6$ earthquakes, as shown in Figure 5. Although the scale changes because of the higher average stress drops for the larger earthquakes, the regional patterns remain roughly the same. Second, we focused on the median stress drops within the two boxes highlighted in these figures, which surround examples of regions with lower-than-average stress drop (175 events in northern box) and higher-than-average stress drop (48 events in southern box). The ratio of median stress drop between these two boxes is nearly constant for four different M_L bins (ratios of 2.6, 2.8, 3.0, and 2.3 for M_L = 1–1.5, 1.5–2, 2–2.5, and 2.5–3, respectively). A bootstrap resampling test indicates that these differences are statistically significant with greater than 99% confidence

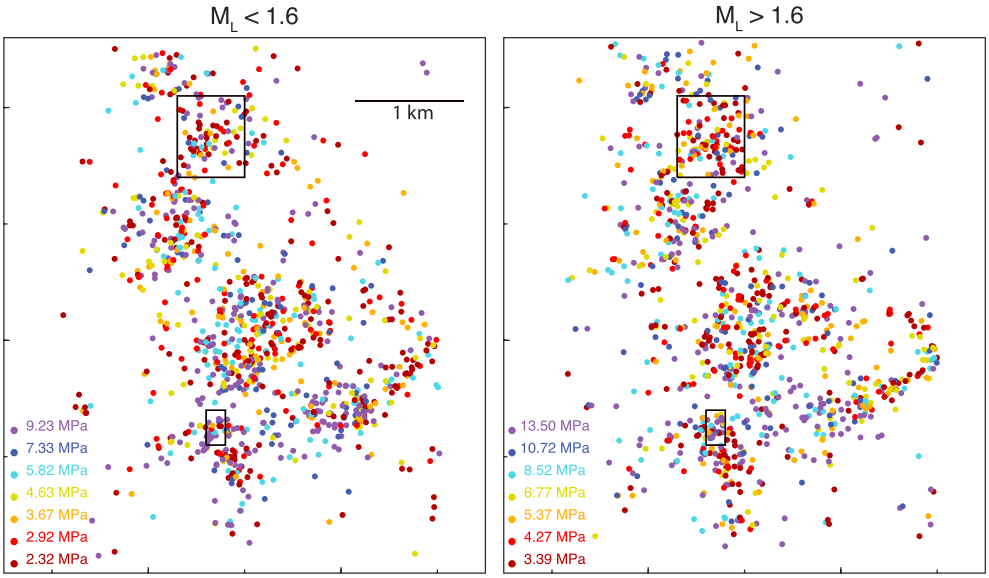

Figure 5. A comparison of stress drop estimates for earthquakes with local magnitudes less than 1.6 (left) and greater than 1.6 (right), again using the global empirical Green's function of Figure 3b.

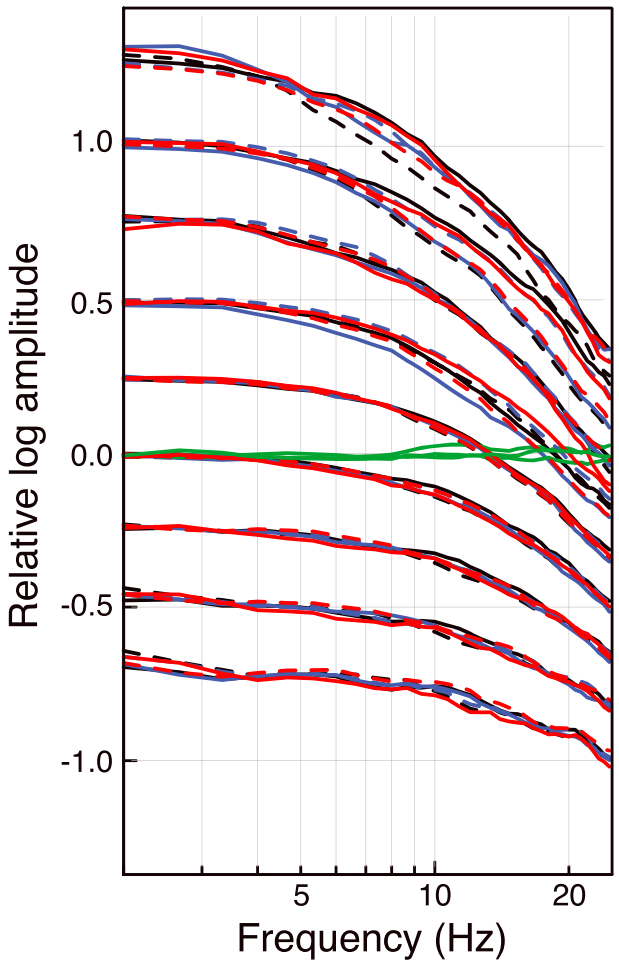

Figure 6. A comparison of event term stacks for spatially separated halves of the events, divided by depth (black), longitude (blue), and latitude (red). The dashed lines show the event halves with lesser depth, longitude, or latitude. The three green lines show the average differences between the two halves for the smallest seven moment bins. Event terms have all been corrected for the global EGF function for the non-self-similar Brune fit.

for the three smaller magnitude bins and with 98% confidence for the M_L = 2.5–3 bins (although this larger bin contains only 13 and 1 event for the low and high stress drop regions, respectively). For comparison, using individual event stress drops estimated after correcting for the EGF from the self-similar model with $n = 1.66$ (Figure 3d), the ratios between the regions are 3.4, 4.7, 4.1, and 3.3, respectively.

Because our entire seismicity cluster spans such a small region (6 km × 6 km × 6 km), it is unlikely that these spatial differences in median stress drop are caused by path differences not taken into account with our single global EGF, consistent with the fact that we do not observe any systematic change in average stress drop with latitude, longitude, or depth within our seismicity box. To further check the validity of the single EGF assumption, we performed three tests in which we divided the event terms in half by latitude, longitude, and depth (based on the coordinate midpoint), and then stacked the event terms in bins of constant moment. For comparison to Figure 3, we corrected the stacks for the global EGF function for the non-self-similar Brune fit. The results are plotted in Figure 6, together with the average differences between the two halves. Although differences are seen in the larger moment bins, reflecting variations among the relatively small number of events in these bins, the results agree closely for the smaller moment bins. The average difference between the two halves (see green lines in 6) is quite small, much less than the differences among the different global EGF function shown in Figure 3. This further confirms the validity of assuming a single global EGF function, even though determining its exact shape is challenging.

In addition, any near-source variations in attenuation would affect the high frequencies of all earthquakes by the same amount, which would cause a much larger change in the estimated stress drops of small earthquakes compared to large earthquakes. Thus, the fact that the spatial stress drop variations are roughly constant as a function of magnitude is more consistent with true variations in source properties than small-scale changes in attenuation structure. The stability of our results as a function of magnitude is important because it suggests that spatial variations in average earthquake source properties can be mapped using the much more numerous small earthquakes and the results will be predictive of large earthquake behavior in the same regions.

4. Application of Spectral Ratio Fitting Method

For test purposes, we assume that the seismicity cluster is small enough for any events to be considered viable EGF events for any others. We begin by selecting 52 target events with $2.7 \leq M_L \leq 3.1$ and 258 smaller EGF events of $1.0 \leq M_L \leq 1.2$. As discussed above, we do not require that the EGF events have high correlation coefficients with the target events or have similar focal mechanisms. In this way, we maximize the number of EGF events and facilitate direct comparisons with the global EGF results. We then compute target-to-EGF-event spectral ratios in two different ways: (1) We stack the EGF event terms from spectral decomposition (see previous section) and subtract the EGF stack from each of the target event terms. (2) Using the original raw *P* wave spectra, for each target event, we identify the recording stations with spectra that meet our SNR criteria and then search the EGF event spectra to find spectra from the same stations that also meet the SNR requirements. We then compute the spectral ratio of every matching station spectra and stack (average) the log ratios, using two different weighting schemes.

Figure 7 plots the spectral ratios for eight examples of the 52 target events, comparing the event term stacking approach (black lines) to the common-station stacking approach (red lines). The solid red line is the simple average of all the individual spectral ratios. The dashed red line is the weighted average, in which each ratio is inversely weighted by the total number of ratios present for that station, which has the effect of giving

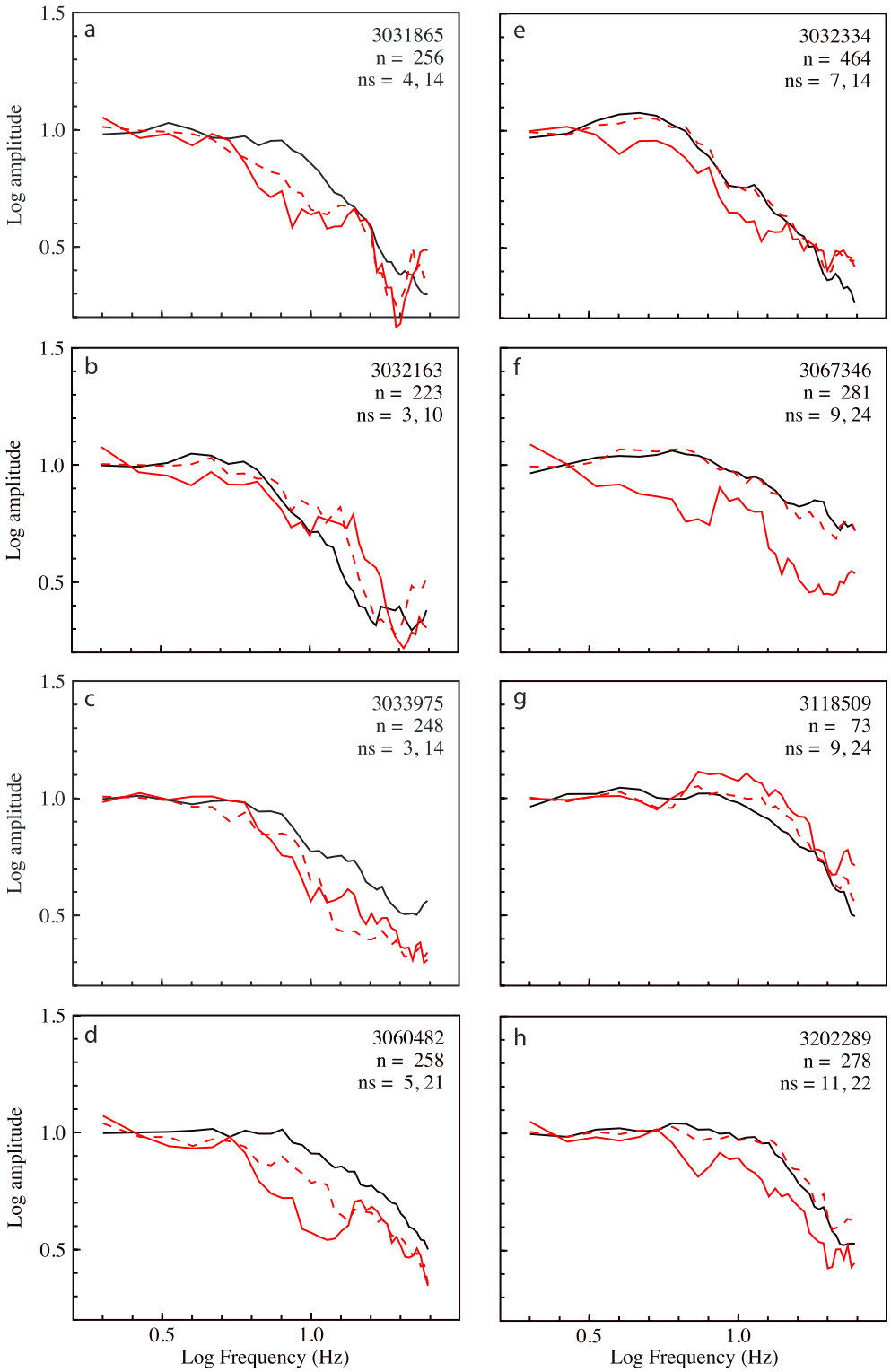

Figure 7. Spectral ratio stacks of eight different target events (M_L = 2.7 to 3.1) to 258 smaller events (M_L = 1 to 1.2) are shown in the panels labeled (a–h). Black lines show spectral decomposition event term ratio stacks; red lines show common-station spectral ratio stacks. The target event id and the total number, *n*, of common station ratios are plotted in each panel. Also labeled are the number of unique stations, *ns*, for the ratio stack and the target event term, respectively. The solid red lines are the averages of all the individual spectral ratios; the dashed red lines are averages weighted inversely by the total number of ratios per station. Axes are in $\log_{10}$ frequency.

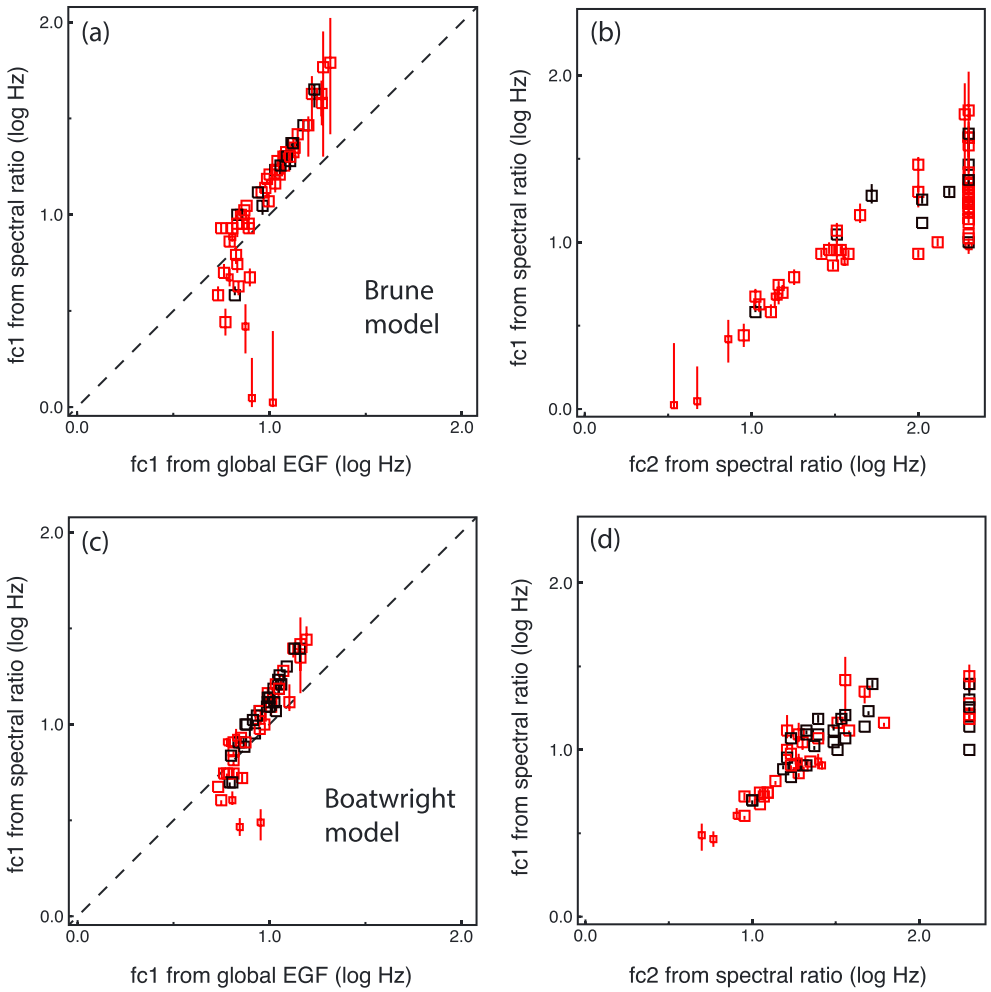

Figure 8. (a) Target event corner frequency estimates, plotting f_{c1} from the spectral ratio fit versus f_c from the fit to the global-EGF-corrected event terms from spectral decomposition. Symbols indicate the misfit level in the spectral ratio fit. The best fits (rms < 0.03) are plotted as black squares, next best (rms < 0.06) are plotted as large red squares, and the worst fits (rms > 0.06) are plotted as small red squares. (b) f_{c1} versus f_{c2} from the spectral ratio fit for the 52 target events. Symbols as in part (a). Axes are in $\log_{10}$ frequency. The top panels (a and b) assume the Brune model in performing the fits; the lower panels (c and d) are for the Boatwright model. rms = root-mean-square; EGF = empirical Green's function.

each station equal weight in the average. In general, we find that the weighted average of the raw spectral ratios produces better agreement with the event term ratio method. The difference between the weighted and unweighted averages is often quite large, reflecting the fact that one or two stations often dominate the total count of raw spectral ratios. For example, Figure 7e plots results for target event 3032334 ($M_L = 2.75$). There are 464 spectral ratios from seven different stations, but 391 of them are from just two stations (GTM and TPC). In the simple unweighted stack, these stations will receive excessive weight and the result will not be a good approximation to the spherically averaged properties of the source. The weighted ratio stack for this event agrees much better with the spectral decomposition event term ratio. We also experimented with more robust stacking methods than simple averages, but found that these did not make much difference compared to the weighted versus unweighted averages.

Poorer agreement between the methods is found for target event 3031865 ($M_L = 3.01$; Figure 7a). In this case, there are 256 spectral ratios, but from only four different stations, and 214 are from station GTM. In contrast, the event term computed from spectral decomposition for this event is derived from 14 different stations and presumably represents a better spherical average of the source. This highlights a limitation of the raw spectra stacking approach. The target events may have been recorded by many stations with good SNR, but a station is not used if there is not an EGF event with good SNR at the same station. The EGF events

are much smaller magnitude than the target and their records typically have poorer SNR, so only some of the stations available for the target event are also available for at least one EGF event. The result is that the spectral ratio stack does not use all of the good SNR spectra for the target event. In contrast, the event terms from spectral decomposition are derived from all of the good SNR spectra recording each event. Regardless of the number of stations, stacking over a large number of EGF events improves the stability of the results by reducing the influence of the variability of individual EGF spectra (Abercrombie, 2015). However, the same target event spectrum contributes to the ratio stack for each station and thus if only a limited number of stations are available the results will suffer from poor spherical averaging around the focal sphere regardless of how many EGF events are analyzed. In this case, the spectral decomposition approach often provides a better spherical average because it includes spectra from more stations recording the target event.

Overall, at least for this data set, the event term ratios exhibit smoother behavior that more closely resembles model predictions. The weighted raw ratio stacks are generally better behaved than the unweighted stacks and agree reasonably well with the event term ratios when more than about five unique station ratios are available (e.g., panels e, f, g, and h). However, when fewer than about five unique station ratios are available (e.g., panels a, c, and d), even the weighted ratio stacks often show poor agreement with the event term ratios, presumably because of their limited spherical averaging and the different numbers of stations used in the numerator for the two methods. This comparison emphasizes the importance of ensuring a sufficient number of stations are used for the smallest magnitude stacks. To ease comparison with the global EGF results from the previous section, we will use the event term ratios to calculate the corner-frequency fits in the discussion that follows.

Using the event term ratios for the 52 target events, we fit for f_{c1} and f_{c2} using equation (9). For consistency with our global EGF analysis, we apply a $1/f$ weight in defining the misfit, so as to give equal weight in log frequency, and use the Brune model ($\gamma = 1$). Figure 8a plots these f_{c1} values versus those obtained from the global EGF approach, in this case using the non-self-similar Brune model (used for Figures 3b, 4, and 5). The results are clearly correlated, but the absolute agreement is poor; the spectral ratio estimates are systematically higher and show a greater range of values, even when the comparison is restricted to the best fitting spectral ratio models. Somewhat better agreement is obtained when the Boatwright model is applied, with both methods yielding f_{c1} estimates with less scatter (Figure 8c).

Some insight into the origin of the poor agreement is shown in Figures 8b and 8d, which plot f_{c1} versus f_{c2} for the spectral ratio fits. The f_{c1} and f_{c2} values are clearly correlated, with higher target event corner frequencies associated with higher corner frequencies for the EGF event stack. But in this case, the same EGF events are used to compute each target event spectral ratio, so they should have the same average corner frequency. Although the f_{c2} values are not used to estimate stress drops, their variability is a source of bias in the target event corner frequencies. The bias is particularly apparent when f_{c2} is anomalously low, which results in a strong correlation between f_{c1} and f_{c2} and poor agreement of f_{c1} with the global EGF estimates. This same effect of underestimation of f_{c1} was observed by Abercrombie (2015) and Ruhl et al. (2017) as a consequence of limited bandwidth; most of the corner frequencies calculated here are unfortunately, too close to the high frequency signal limit to be considered reliable based on their recommendations. When the f_{c2} values are at or above the highest frequency in the data, then the results of the two methods are better correlated, though with a systematic offset.

Figure 9 illustrates this for two example target events, comparing the Brune model fits obtained from the global-EGF-corrected spectra with those from the spectral ratio method. Because f_{c2} is allowed to vary in the fits to the spectral ratios, there is an additional degree of freedom in performing the fits. The result is that changes to f_{c2} are often driven by the nature of the misfit to the target event spectra. The additional degree of freedom means that f_{c2} can vary to match troughs and bumps in the spectral ratios produced by complexity in the original earthquake source spectra. Such features are not uncommon in real data; for example, Uchide and Imanishi (2016) demonstrated that many earthquakes exhibit significant variation from the smooth model spectra assumed here (equation (1)), and complex spectra and relative source time functions are observed in many locations where small earthquakes are well recorded (e.g., Abercrombie et al., 2016; Ruhl et al., 2017), similar to the complexities commonly observed for larger earthquakes.

As shown in the left column for event 7048135, when the target event spectral corner is sharper than the model (in this case, Brune), with a bump around 10 Hz, both f_{c1} and f_{c2} shift to higher values. In contrast (right column), when the target event corner is smoother than the model, both f_{c1} and f_{c2} shift to lower

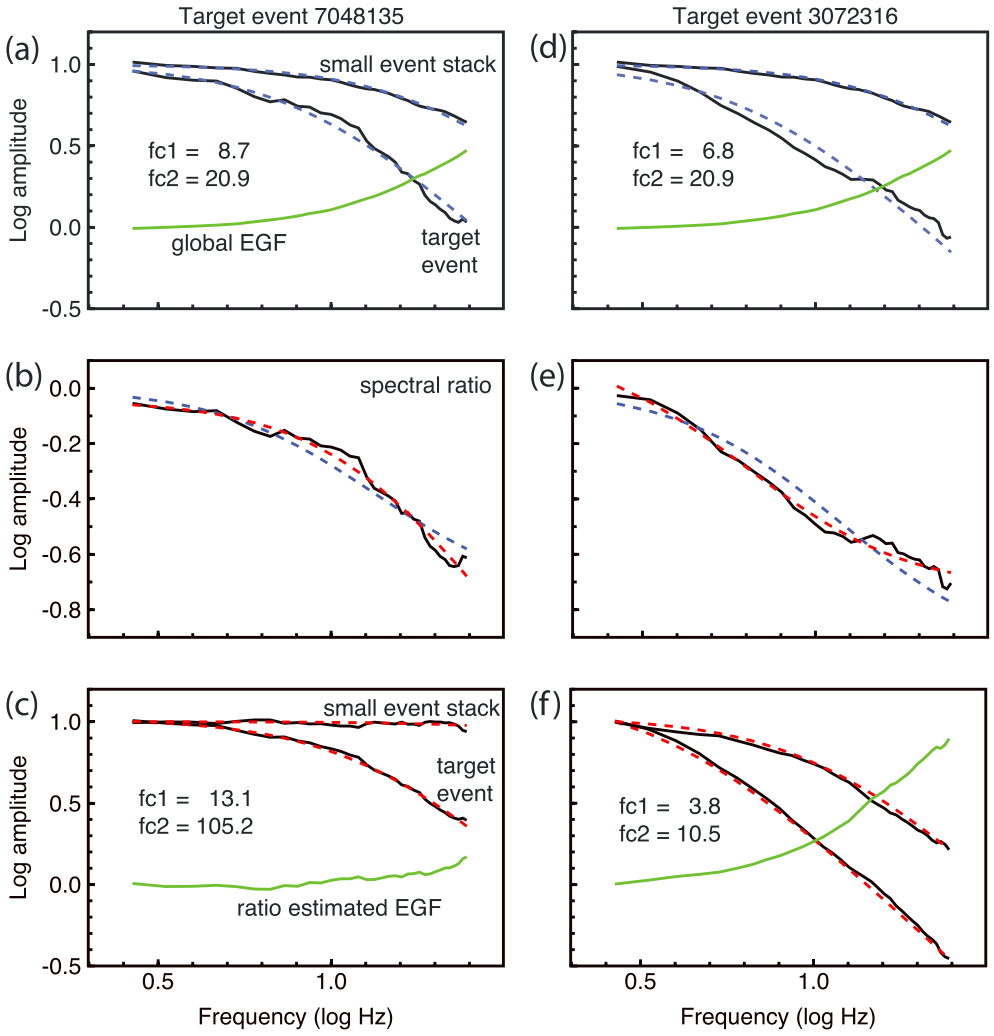

Figure 9. A comparison of Brune model fits from the global EGF approach to the spectral ratio method for two different target events. (a, d) event terms for the target event and the EGF event term stack for the 258 smaller earthquakes, each corrected for the global EGF function (green line). The fits obtained by the best fitting f_c values (labeled as f_{c1} and f_{c2} for the target and EGF event stack, respectively) are plotted as the blue dashed lines. (b, e) The event term spectral ratio (solid line), compared to the best fitting model over all possible values of f_{c1} and f_{c2} (red dashed line) and the predicted fit from the global EGF fits from the top panel (blue dashed line). (c, f) The predicted fits to the target and EGF event stack from the spectral ratio fit (red dashed lines), after correcting for a best fitting EGF function (green curve). The f_{c1} and f_{c2} values from the spectral ratio fit are labeled; these were used to compute the red dashed curves in the middle row. Axes are in $\log_{10}$. EGF = empirical Green's function.

values. In fitting a single spectral ratio, the modeling cannot distinguish between a bump at 10 Hz being a real feature of the source spectrum or an effect of an upward shift in f_{c2}. However, in this case, by comparing to other spectral ratios derived from the same EGF events, we know that f_{c2} should not be near 100 Hz as implied by the best fit to the ratio plotted in Figure 9c. The fit to the spectral ratio curve is better when both f_{c1} and f_{c2} are allowed to vary (as shown in the middle row of Figure 9, but the quality of the spectral ratio fit is a poor guide to the reliability of the f_{c1} values. The inferred EGF functions from the spectral ratio fits for the two target events are very different (green curves in bottom panel), so that the inferred EGF-corrected spectra for the small event stack (the same in each case) are also very different. For comparison, Figure 10 shows Boatwright model fits for these two events. In this case, the difference in f_{c2} for the best fit to the spectral ratio for the two events is less than for the Brune model fits but still leads to a substantial bias in the f_{c1} values. All methods used identify event 3072316 as having a lower corner frequency than event 7048135, implying that relative corner frequency measurements are less model dependent.

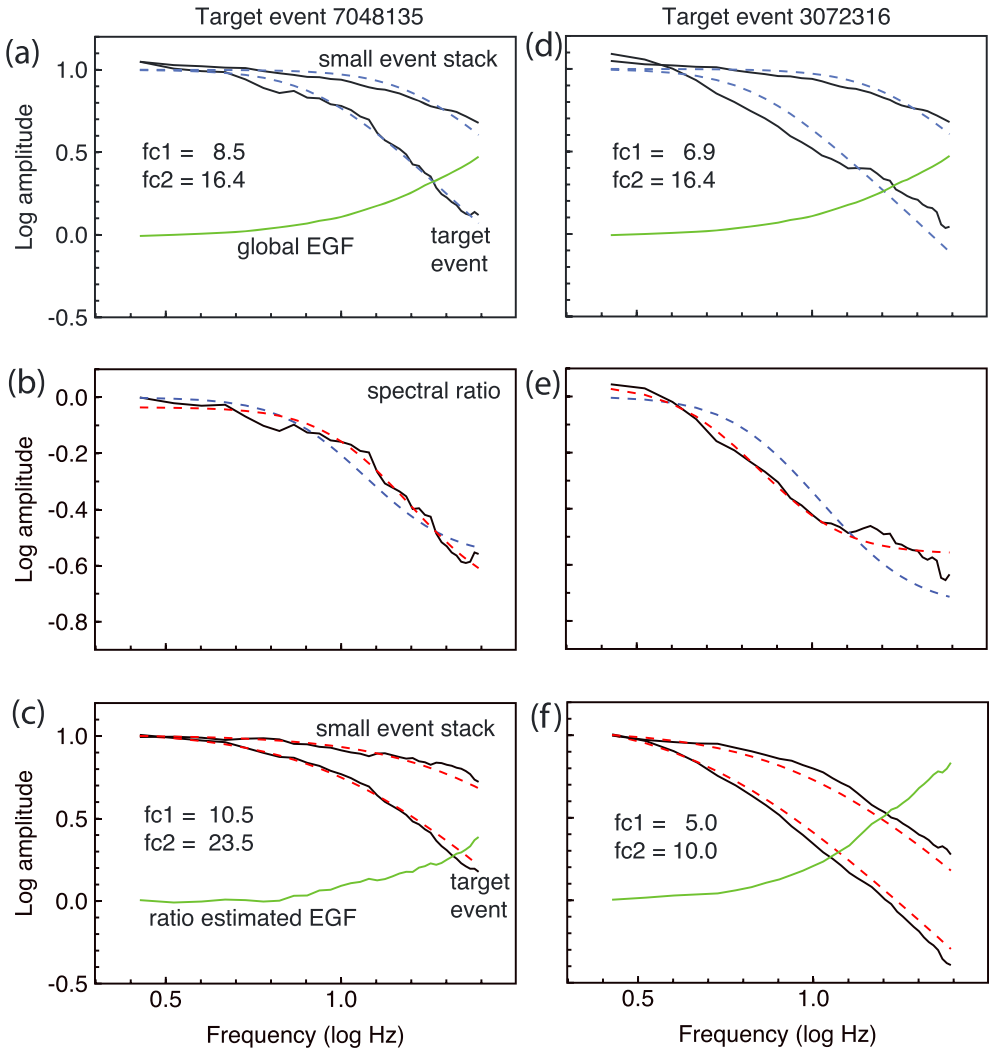

Figure 10. A comparison of Boatwright model fits from the global empirical Green's function approach to the spectral ratio method for two different target events. Panels are as described in Figure 9.

For our test analysis here, because we use the same set of EGF events for each target event, we can stabilize the spectral ratio approach by forcing f_{c2} to a fixed value. For the Brune model, by using $f_{c2} = 21$ Hz (the value from the global EGF-corrected EGF event term stack), we obtain good agreement between the ratio-fitted and the global-EGF-fitted values for target event corner frequency (f_{c1}), as shown in Figure 11b. If f_{c2} is fixed to a smaller value, then f_{c1} is shifted to lower values (Figure 11a), and if f_{c2} is fixed to a larger value, then f_{c1} is shifted to higher values (Figure 11c). For the Boatwright model (see right column of Figure 11), the best agreement with the global-EGF-fitted values is obtained by using $f_{c2} = 15$ Hz. The difference in total rms misfit for the six examples shown in Figure 11 is only ~10%; some individual spectra are better fit with the Boatwright model, but the Brune model has a marginally better fit to the whole data set, misfit decreasing with increasing f_{c2}. The fractional shift in f_{c1} is about 50% to 80% of the shift in the fixed value of f_{c2}, with a larger fractional shift occurring as f_{c2} moves to smaller values (see Figure 8).

Please note that the global-EGF corner frequencies shown here are not necessarily correct, as they are subject to uncertainties in the global EGF previously discussed. Our point here is simply that the spectral ratio and global-EGF corner frequencies for the target events can be made reasonably consistent by forcing the EGF events to have the same average corner frequency. For both methods, the relative f_{c1} are much better resolved than the absolute values.

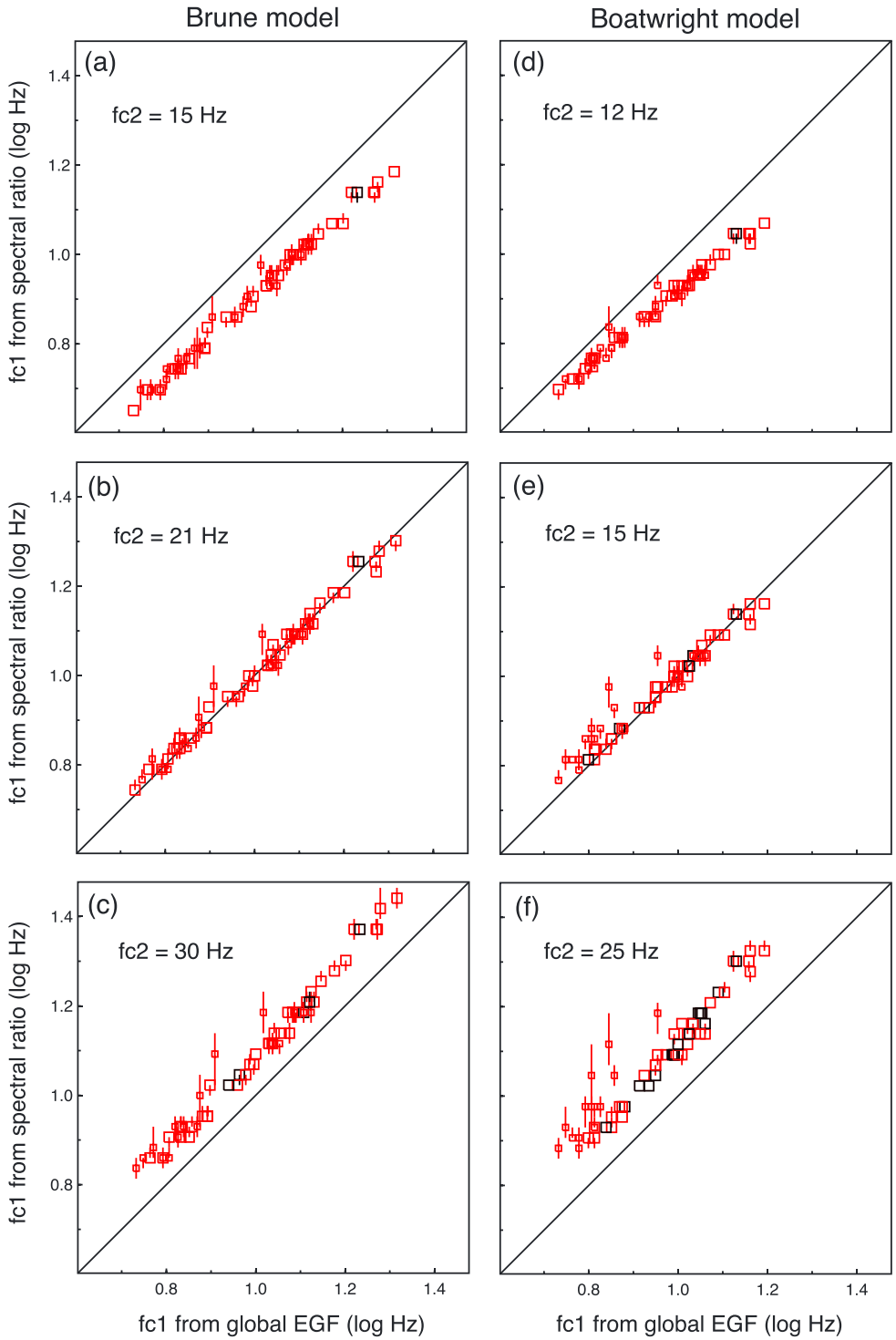

Figure 11. Similar to Figures 8a and 8c but with f_{c2} fixed at specific values, rather than being allowed to vary to a best fitting value. Constraining the corner frequency of the EGF event term stack in this way produces a much better agreement with the global EGF derived target event corner frequencies, with the best agreement seen in the middle row where f_{c2} is set to the value from the global EGF-corrected EGF event term stack. Symbols indicate the misfit level in the spectral ratio fit. The best fits (rms < 0.03) are plotted as black squares, next best (rms < 0.06) are plotted as large red squares, and the worst fits (rms > 0.06) are plotted as small red squares. Axes are in $\log_{10}$ frequency. EGF = empirical Green's function.

5. Discussion and Conclusions

Source studies of small to moderate sized earthquakes often rely on EGF estimates to correct the records for attenuation and other path effects. Here, we explore the stability and consistency of two common approaches for EGF analysis and corner frequency estimation and find that both are affected by the limitations of the available data. By using the same set of EGF events for different target events, we show that placing no constraints on f_{c2} in the spectral ratio method will introduce biases in the target event corner frequencies f_{c1}. These result from uncertainties in the actual spectra (e.g., limited station selection) and source complexity such that the true source spectra do not exactly match the smooth model curves assumed in fitting the spectra. Thus, when identical EGF events are used for multiple target events, their average corner frequency (f_{c2}) should be fixed so that relative differences in target event corner frequency (f_{c1}) are caused by real differences in the target event spectra rather than changes in the assumed EGF. In our case, we fixed f_{c2} to the value obtained from our global-EGF results. If a global-EGF analysis is not available, f_{c2} could be estimated by simultaneously fitting all the target event spectral ratios. The resulting value may not be particularly well constrained, as there will be trade-offs in the misfit properties similar to those discussed in section 3 for the global EGF analysis. However, a single f_{c2} value is nonetheless preferred, as it will produce more reliable results for the relative variations in the target event corner frequencies.

Of course, many studies use a custom set of EGF events for each target event and some variation in f_{c2} should be expected in this case. However, placing no constraints on f_{c2} can lead to biased estimates of f_{c1}, as shown in Figures 8 and 9. The quality criteria introduced by Abercrombie et al. (2016) are aimed at decreasing this bias, but placing reasonable constraints on f_{c2} would seem a sensible way to improve the results, especially if f_{c2} is for a stack of EGF events. The mean stress drop (when calculated using the same k value) varies by less than a factor of 10 between most studies. Hence, constraining f_{c2} to within a factor of 2, based on the predicted stress drop would not seem to overly prescriptive and would help prevent earthquake source complexity being erroneously modeled. We do not test this idea here, but plan to experiment with this and other approaches for analysis of large seismicity regions for which possible spatial variations in the EGF need to be taken into account.

When large numbers of events of varying magnitudes are available in a compact region, the spectral decomposition and global-EGF-fitting method has some advantages. It uses all the available good SNR data for every event and provides a unified approach to estimating relative event moments and a single global EGF function that is self-consistent among all the earthquakes. Although computation of the global EGF function is model dependent, it can be used to correct the event terms to obtain estimates of the true source spectra of all the individual events prior to any fits for individual event corner frequencies. Unlike traditional EGF approaches, it obtains source spectral estimates for all the earthquakes, not just the larger magnitude earthquakes selected as target events. Although the corner frequency estimates for the smaller earthquakes are not as well constrained as those for the larger earthquakes, the measurements are more consistent than those from traditional EGF approaches (e.g., Abercrombie, 2013). The smaller earthquakes are much more numerous and exhibit spatial variations consistent with those seen for the larger earthquakes, at least for the test data set analyzed here. A disadvantage of the spectral decomposition approach is that it cannot be used to obtain time domain source time functions. These can be used to obtain alternative estimates of source duration (and hence stress drop), and also source directivity and complexity (e.g,. Abercrombie et al., 2017; Fan & McGuire, 2018).

The global EGF function itself is subject to considerable uncertainty, despite the good fits that we obtain to the moment-binned event term stacks, because of trade-offs among the model parameters. As shown in Figure 3, these include the $\Delta\sigma(M_0)$ scaling parameter, ϵ, the high-frequency falloff rate, n, and the absolute stress drop of the smallest event term stack. These results are of course specific to our data set with its magnitude range and 2.5- to 25-Hz bandwidth. However, similar trade-offs were noted by Trugman and Shearer (2017) for other regions in Southern California, suggesting that it is fundamentally difficult to constrain the EGF with a limited frequency bandwidth and a purely empirical approach. A comprehensive synthetic experiment to investigate the moment range and the frequency range required to resolve these ambiguities would be a useful next step. The existing trade-offs make any absolute comparisons between EGF-corrected source spectra obtained for different regions subject to considerable uncertainty. But this does not alter the ample observational evidence that distance-corrected seismograms from earthquakes of similar moments contain different amounts of high-frequency energy and that these variations exhibit spatially coherent

patterns (e.g., Oth, 2013; Shearer et al., 2006; Trugman & Shearer, 2018). Of course, some of these variations could be due to uncorrected differences in near-source attenuation or other path effects rather than true source differences. Here we show that spatially coherent variations in high-frequency energy are present even within a very compact cluster of seismicity, where EGF differences are unlikely, and that these source variations are robust with respect to earthquake moment.

The spectral ratio fitting method can be applied to the event term ratios from spectral decomposition and for our data set this approach appears to have some advantages over stacking raw spectral ratios at common stations because it uses all of the available stations for the target events rather than just the stations that also have good SNR records for the smaller-magnitude EGF events. The spectral ratio method yields stable results for our data only if the upper corner frequency, f_{c2}, is not allowed to vary separately for each target event. This is at least partially because our 25-Hz maximum frequency does not permit reliable determination of corner frequency for the small-magnitude earthquakes (Abercrombie, 2015; Ruhl et al., 2017). Simultaneously fitting all closely located target and smaller events in a more constrained inversion should produce more reliable results (e.g., Hough, 1997; Imanishi & Ellsworth, 2006; Kwiatek et al., 2014). In addition, the difference in long-period levels obtained from the ratio fit could be used to compute relative moment and test for self-similarity (i.e., whether f_{c1} and f_{c2} are consistent with $f_c \propto M_0^{-1/3}$, as is done in spectral decomposition and global EGF analyses).

Another approach is to simply assume a fixed stress drop for the smaller-magnitude EGF events and then predict their corner frequency based on their estimated moment and a theoretical model. This was done by Baltay et al. (2011, 2010) for their coda-based analyses and has the advantage of stabilizing the inversion for the EGF and the source spectra of the larger earthquakes, but with the disadvantage of eliminating the possibility of resolving any differences in the small-earthquake stress drops. Our results suggest that lateral variations in average small-event stress drop are correlated with those at larger magnitudes, at least for our test region. However, the bias introduced into the larger-magnitude stress drops by assuming the wrong average stress drop for the small earthquakes is proportionally much less than error in the small-event stress drops themselves, owing to the lower corner frequencies for the larger events. Fixing the small-event average stress drop also has the advantage that it makes it more likely that any differences among distinct regions seen in the average stress drop of larger events are real, rather than an artifact of using an inaccurate EGF.

Our focus on a single compact seismicity cluster has the advantage that a fixed EGF is likely a good approximation for our entire data set, so that we can focus on differences in the analysis methods that are driven by earthquake source properties and not uncorrected path effects. We specifically limited our depth range to remove any systematic variation in spectral shape. Addressing larger questions, such as the depth dependence of average stress drop, or the reliability of big differences in average stress drops for nearby regions noted in some recent studies (e.g., Oth, 2013; Trugman & Shearer, 2017), will require analysis of larger seismicity clusters, and this is planned for future work.

In summary, the global EGF approach uses all good recordings to obtain consistent relative moments and corner frequencies for densely clustered earthquakes. However, for the magnitude and frequency range of the Southern California regional network data, trade-offs among the different model parameters, including non-self-similar scaling, high-frequency falloff rate, and the estimated EGF introduce uncertainty in the absolute values of the corner frequencies (and computed stress drops). This makes it difficult to compare stress drops reliably across large regions where a single global EGF is likely inaccurate, but separately computed or spatially varying EGFs suffer from the model parameter trade-offs. Spectral ratio analysis is more suited to detailed analysis of the best recorded earthquakes, for example, directivity using time domain measurements, and for smaller data sets that are insufficient for a global EGF approach. However, constraints are needed to ensure an unbiased station distribution in event averages and on the average corner frequency of the smaller events to prevent it from affecting the target earthquake. When few earthquakes are available in an analysis then any interpretation should include both the formal statistical fitting errors, and the likely realistic errors extrapolated from resolution test studies such as this one; a combined inversion of nearby events using similar EGFs is another recommended approach such as the multi-EGF method (e.g., Hough, 1997; Ide et al., 2003; Imanishi & Ellsworth, 2006; Kwiatek et al., 2014).

Finally, it is important to recognize that "stress drop" may be a poor parameter to quantify variations in earthquake source spectra, as it is highly model dependent. Corner frequency is a parameter closer to the actual data, but it also can be computed in different ways. From the observational perspective, the main

challenge is to find reliable approaches to removing path effects so as to obtain unbiased estimates of the true source spectra and their takeoff angle dependence. In this respect, other methods, such as the second moment estimates (e.g., Fan & McGuire, 2018; McGuire, 2004) will likely also prove useful, but they too are limited by the quantity and frequency range of the available data. In any case, the vast amount of high-quality data recorded by modern seismic networks from massive catalogs of earthquakes motivates the development of analysis methods that can fully exploit all of the information available in their spectra.

Acknowledgments
We thank the personnel of the USGS/Caltech Southern California Seismic Network (SCSN) who pick and archive the seismograms and the Southern California Earthquake Center (SCEC, https://www.scec.org) for distributing the data used in this study. Funding for this research was provided by NEHRP/USGS grant G18AP00024 and by SCEC under grants 17041 and 18086. SCEC is funded by NSF Cooperative Agreement EAR-1033462 and USGS Cooperative Agreement G12AC20038. D. Trugman acknowledges institutional support from the Laboratory Directed Research and Development (LDRD) program at Los Alamos National Laboratory. This paper is SCEC contribution number 8916.

References

Abercrombie, R. E. (1995). Earthquake source scaling relationships from 1 to 5 ML using seismograms recorded at 2.5-km depth. *Journal of Geophysical Research*, *100*(B12), 24,015–24,036.

Abercrombie, R. E. (1996). The magnitude-frequency distribution of earthquakes recorded with deep seismometers at Cajon Pass, Southern California. *Tectonophysics*, *261*(1), 1–8.

Abercrombie, R. E. (2013). Comparison of direct and coda wave stress drop measurements for the Wells, Nevada, earthquake sequence. *Journal of Geophysical Research: Solid Earth*, *118*, 1458–1470. https://doi.org/10.1029/2012JB009638

Abercrombie, R. E. (2014). Stress drops of repeating earthquakes on the San Andreas Fault at Parkfield. *Geophysical Research Letters*, *41*, 8784–8791. https://doi.org/10.1002/2014GL062079

Abercrombie, R. E. (2015). Investigating uncertainties in empirical Green's function analysis of earthquake source parameters. *Journal of Geophysical Research: Solid Earth*, *120*, 4263–4277. https://doi.org/10.1002/2015JB011984

Abercrombie, R. E., Bannister, S., Ristau, J., & Doser, D. (2016). Variability of earthquake stress drop in a subduction setting, the Hikurangi Margin, New Zealand. *Geophysical Journal International*, *208*, 306–320.

Abercrombie, R. E., Poli, P., & Bannister, S. (2017). Earthquake directivity, orientation, and stress drop within the subducting plate at the Hikurangi margin, New Zealand. *Journal of Geophysical Research: Solid Earth*, *122*, 10,176–10,188. https://doi.org/10.1002/2017JB014935

Abercrombie, R. E., & Rice, J. R. (2005). Can observations of earthquake scaling constrain slip weakening? *Geophysical Journal International*, *162*(2), 406–424.

Andrews, D. (1986). Objective determination of source parameters and similarity of earthquakes of different size. *Earthquake Source Mechanics*, *37*, 259–267.

Baltay, A., Ide, S., Prieto, G., & Beroza, G. (2011). Variability in earthquake stress drop and apparent stress. *Geophysical Research Letters*, *38*, L06303. https://doi.org/10.1029/2011GL046698

Baltay, A., Prieto, G., & Beroza, G. C. (2010). Radiated seismic energy from coda measurements and no scaling in apparent stress with seismic moment. *Journal of Geophysical Research*, *115*, B08314. https://doi.org/10.1029/2009JB006736

Bindi, D., Pacor, F., Luzi, L., Massa, M., & Ameri, G. (2009). The Mw 6.3, 2009 L'Aquila earthquake: Source, path and site effects from spectral analysis of strong motion data. *Geophysical Journal International*, *179*(3), 1573–1579.

Boatwright, J. (1980). A spectral theory for circular seismic sources: Simple estimates of source dimension, dynamic stress drop, and radiated seismic energy. *Bulletin of the Seismological Society of America*, *70*(1), 1–27.

Boyd, O. S., McNamara, D. E., Hartzell, S., & Choy, G. (2017). Influence of lithostatic stress on earthquake stress drops in North America. *Bulletin of the Seismological Society of America*, *107*(2), 856–868.

Brune, J. N. (1970). Tectonic stress and the spectra of seismic shear waves from earthquakes. *Journal of Geophysical Research*, *75*(26), 4997–5009.

Calderoni, G., Rovelli, A., Ben-Zion, Y., & Di Giovambattista, R. (2015). Along-strike rupture directivity of earthquakes of the 2009 L'Aquila, central Italy, seismic sequence. *Geophysical Journal International*, *203*(1), 399–415.

Eshelby, J. D. (1957). The determination of the elastic field of an ellipsoidal inclusion, and related problems. *Proceedings of the Royal Society London A*, *241*(1226), 376–396.

Fan, W., & McGuire, J. J. (2018). Investigating microearthquake finite source attributes with IRIS Community Wavefield Demonstration Experiment in Oklahoma. *Geophysical Journal International*, *214*(2), 1072–1087.

Frankel, A. (1982). The effects of attenuation and site response on the spectra of microearthquakes in the northeastern Caribbean. *Bulletin of the Seismological Society of America*, *72*(4), 1379–1402.

Hanks, T. C., & Boore, D. M. (1984). Moment-magnitude relations in theory and practice. *Journal of Geophysical Research*, *89*(B7), 6229–6235.

Hardebeck, J. L., & Shearer, P. M. (2003). Using S/P amplitude ratios to constrain the focal mechanisms of small earthquakes. *Bulletin of the Seismological Society of America*, *93*(6), 2434–2444.

Hauksson, E., Yang, W., & Shearer, P. M. (2012). Waveform relocated earthquake catalog for Southern California (1981 to June 2011). *Bulletin of the Seismological Society of America*, *102*(5), 2239–2244.

Hough, S. (1997). Empirical Green's function analysis: Taking the next step. *Journal of Geophysical Research*, *102*(B3), 5369–5384.

Huang, Y., Beroza, G. C., & Ellsworth, W. L. (2016). Stress drop estimates of potentially induced earthquakes in the Guy-Greenbrier sequence. *Journal of Geophysical Research: Solid Earth*, *121*, 6597–6607. https://doi.org/10.1002/2016JB013067

Hutchings, L., & Viegas, G. (2012). Application of Empirical Green's Functions in Earthquake Source, Wave Propagation and Strong Ground Motion Studies, Earthquake Research and Analysis - New Frontiers in Seismology, Sebastiano D'Amico, IntechOpen. https://doi.org/10.5772/28189, https://www.intechopen.com/books/earthquake-research-and-analysis-new-frontiers-in-seismology/application-of-empirical-green-s-functions-in-earthquake-source-wave-propagation-and-strong-ground-m

Hutton, K., Woessner, J., & Hauksson, E. (2010). Earthquake monitoring in southern California for seventy-seven years (1932–2008). *Bulletin of the Seismological Society of America*, *100*(2), 423–446.

Ide, S., & Beroza, G. C. (2001). Does apparent stress vary with earthquake size? *Geophysical Research Letters*, *28*(17), 3349–3352.

Ide, S., Beroza, G. C., Prejean, S. G., & Ellsworth, W. L. (2003). Apparent break in earthquake scaling due to path and site effects on deep borehole recordings. *Journal of Geophysical Research*, *108*(B5), 2271. https://doi.org/10.1029/2001JB001617

Imanishi, K., & Ellsworth, W. L. (2006). Source scaling relationships of microearthquakes at Parkfield, CA, determined using the SAFOD pilot hole seismic array. *Earthquakes: Radiated Energy and the Physics of Faulting*, *170*, 81–90.

Kaneko, Y., & Shearer, P. (2014). Seismic source spectra and estimated stress drop derived from cohesive-zone models of circular subshear rupture. *Geophysical Journal International*, *197*, 1002–1015.

Kaneko, Y., & Shearer, P. (2015). Variability of seismic source spectra, estimated stress drop, and radiated energy, derived from cohesive-zone models of symmetrical and asymmetrical circular and elliptical ruptures. *Journal of Geophysical Research: Solid Earth*, *120*, 1053–1079. https://doi.org/10.1002/2014JB011642

Kwiatek, G., Bulut, F., Bohnhoff, M, & Dresen, G. (2014). High-resolution analysis of seismicity induced at Berlín geothermal field, El Salvador. *Geothermics*, *52*, 98–111.

Madariaga, R. (1976). Dynamics of an expanding circular fault. *Bulletin of the Seismological Society of America*, *66*(3), 639–666.

Mayeda, K., & Walter, W. R. (1996). Moment, energy, stress drop, and source spectra of western united states earthquakes from regional coda envelopes. *Journal of Geophysical Research*, *101*(B5), 11,195–11,208.

McGuire, J. J. (2004). Estimating finite source properties of small earthquake ruptures. *Bulletin of the Seismological Society of America*, *94*(2), 377–393.

Mori, J., & Frankel, A. (1990). Source parameters for small events associated with the 1986 North Palm Springs, California, earthquake determined using empirical Green functions. *Bulletin of the Seismological Society of America*, *80*(2), 278–295.

Mueller, C. S. (1985). Source pulse enhancement by deconvolution of an empirical Green's function. *Geophysical Research Letters*, *12*(1), 33–36.

Munafò, I., Malagnini, L., & Chiaraluce, L. (2016). On the relationship between Mw and ML for small earthquakes. *Bulletin of the Seismological Society of America*, *106*(5), 2402–2408.

Oth, A. (2013). On the characteristics of earthquake stress release variations in Japan. *Earth and Planetary Science Letters*, *377*, 132–141.

Oth, A., Bindi, D., Parolai, S., & Di Giacomo, D. (2011). Spectral analysis of K-NET and KiK-net data in Japan, part ii: On attenuation characteristics, source spectra, and site response of borehole and surface stations. *Bulletin of the Seismological Society of America*, *101*(2), 667–687.

Oth, A., Miyake, H., & Bindi, D. (2017). On the relation of earthquake stress drop and ground motion variability. *Journal of Geophysical Research: Solid Earth*, *122*, 5474–5492. https://doi.org/10.1002/2017JB014026

Pacor, F., Spallarossa, D., Oth, A., Luzi, L., Puglia, R., Cantore, L., et al. (2015). Spectral models for ground motion prediction in the L'Aquila region (central Italy): Evidence for stress-drop dependence on magnitude and depth. *Geophysical Journal International*, *204*(2), 697–718.

Prieto, G. A., Shearer, P. M., Vernon, F. L., & Kilb, D. (2004). Earthquake source scaling and self-similarity estimation from stacking *P* and *S* spectra. *Journal of Geophysical Research*, *109*, B08310. https://doi.org/10.1029/2004JB003084

Ross, Z. E., & Ben-Zion, Y. (2016). Toward reliable automated estimates of earthquake source properties from body wave spectra. *Journal of Geophysical Research: Solid Earth*, *121*, 4390–4407. https://doi.org/10.1002/2016JB013003

Ross, Z. E., Ben-Zion, Y., White, M. C., & Vernon, F. L. (2016). Analysis of earthquake body wave spectra for potency and magnitude values: Implications for magnitude scaling relations. *Geophysical Supplements to the Monthly Notices of the Royal Astronomical Society*, *207*(2), 1158–1164.

Ruhl, C., Abercrombie, R., & Smith, K. (2017). Spatiotemporal variation of stress drop during the 2008 Mogul, Nevada, earthquake swarm. *Journal of Geophysical Research: Solid Earth*, *122*, 8163–8180. https://doi.org/10.1002/2017JB014601

Sato, T., & Hirasawa, T. (1973). Body wave spectra from propagating shear cracks. *Journal of Physics of the Earth*, *21*(4), 415–431.

Shearer, P. M., Prieto, G. A., & Hauksson, E. (2006). Comprehensive analysis of earthquake source spectra in Southern California. *Journal of Geophysical Research*, *111*, B06303. https://doi.org/10.1029/2005JB003979

Trugman, D. T., & Shearer, P. M. (2017). Application of an improved spectral decomposition method to examine earthquake source scaling in Southern California. *Journal of Geophysical Research: Solid Earth*, *122*, 2890–2910. https://doi.org/10.1002/2017JB013971

Trugman, D. T., & Shearer, P. M. (2018). Strong correlation between stress drop and peak ground acceleration for recent M 1-4 earthquakes in the San Francisco Bay Area. *Bulletin of the Seismological Society of America*, *108*(2), 929–945.

Uchide, T., & Imanishi, K. (2016). Small earthquakes deviate from the omegasquare model as revealed by multiple spectral ratio analysis. *Bulletin of the Seismological Society of America*, *106*(3), 1357–1363.

Viegas, G., Abercrombie, R. E., & Kim, W.-Y. (2010). The 2002 M5 Au Sable Forks, NY, earthquake sequence: Source scaling relationships and energy budget. *Journal of Geophysical Research*, *115*, B07310. https://doi.org/10.1029/2009JB006799